Unsteady Pressure Measurements on a Simplified High-Lift Configuration of the Common Research Model using Active Flow Control

Keith B. Paschal[1], Michael A. Kegerise[2], Dan H. Neuhart[3], Mehti Koklu[4], and John C. Lin[5]
NASA Langley Research Center, Hampton, VA 23681, USA

The High-Lift Common Research Model (CRM-HL) is a product of the NASA Advanced Air Transport Technology (AATT) Project intended to study various high-lift aerodynamic phenomena including enhanced lift, acoustic noise generation, and optimum placement of leading- and trailing-edge devices. The current study was conducted in the NASA Langley 14- by 22-Foot Subsonic Tunnel (14x22) for the purpose of evaluating enhanced lift through the use of active flow control (AFC). The current paper documents the effect of sweeping-jet actuation combined with steady blowing on a simplified high-lift configuration using unsteady pressure measurements. The time-series parameters for the measurements are documented as well as the data acquisition system used to acquire the data. An uncertainty analysis will be presented in order to document the system performance and provide an estimate of the data quality. Repeatability of the data will be shown along with trends associated with model angle of attack, and also those associated with changes in the nozzle pressure ratio (NPR) of the AFC system.

I. Nomenclature

α	=	angle of attack
AFC	=	active flow control
CRM	=	common research model
f	=	frequency
G	=	nondimensional filter gain
G_{pp}	=	power spectral density of fluctuating pressure
M	=	tunnel Mach number
N	=	number of independent samples
NPR	=	nozzle pressure ratio
p	=	unsteady pressure measurement
Q	=	tunnel dynamic pressure
r	=	order of the statistical moment
s	=	unsteady pressure sensor sensitivity (psi/Volt)
SHL	=	simplified high lift
U	=	uncertainty of the unsteady pressure signal
v	=	voltage signal of the unsteady pressure transducer

[1] Research Scientist, Flow Physics and Control Branch, MS 170
[2] Research Scientist, Flow Physics and Control Branch, MS 170
[3] Research Scientist, Flow Physics and Control Branch, MS 170
[4] Research Scientist, Flow Physics and Control Branch, MS 170, AIAA Member
[5] Senior Research Scientist, Flow Physics and Control Branch, MS 170, AIAA Associate Fellow

II. Introduction

The NASA Advanced Air Transport Technology (AATT) Project is evaluating the use of active flow control (AFC) to enhance the performance of high-lift systems. As a result, a high-lift version of the Common Research Model (CRM-HL) was designed, fabricated, and tested in the NASA Langley 14- by 22-Foot Subsonic Tunnel (14x22). A detailed discussion of the reasoning behind the project's efforts is laid out in Lin et al. [1]. The conventional high-lift configuration (CRM-HL) for the CRM shares leading-edge components with the AFC configuration, which deploys a simplified high-lift (SHL) flap system. The AFC configuration (CRM-SHL-AFC) is equipped with a simple-hinged flap nominally deflected to 50°[1]. The focus of this paper will be on unsteady pressure measurements obtained on the CRM-SHL-AFC configuration.

In addition to the conventional high-lift configuration (CRM-HL) and the simplified high-lift configuration (CRM-SHL-AFC), additional leading-edge components were fabricated to facilitate acoustic testing of the CRM-HL. The model was also designed such that a rigging study could be performed on the conventional leading-edge and trailing-edge devices. The goal of the later study would be to optimize the gap and overhang of the various slats and flaps for the conventional system. Initial testing of the CRM-HL and CRM-SHL-AFC configurations was performed in the summer - fall of 2018 at the Langley 14x22 [1,2]. In addition, a preliminary acoustic investigation was performed in late December of 2018 during that first 14x22 entry. Rigging studies were carried out by Boeing at the QinetiQ 5m wind tunnel in the UK during the fall of 2019 [3].

III. Experimental Setup

Both the CRM-HL and CRM-SHL-AFC configurations have been tested at the NASA LaRC 14x22 [4]. This facility is a closed return, atmospheric wind tunnel with a test section that is 14.5 ft. high, 21.75 ft. wide, and 50 ft. long. The facility has a maximum freestream velocity of 338 ft/s, which corresponds to a maximum dynamic pressure of 144 psf. The maximum unit Reynolds number is 2.2 million per foot. The testing was performed at a freestream Mach number of 0.2 and a corresponding dynamic pressure of approximately 60 psf. Detailed information concerning model dimensions, tunnel instrumentation, and additional measurement techniques such as oil-flow visualization may be found in Lin et al. [1].

The 10%-scale semispan, CRM model is shown in Fig. 1, which depicts the CRM-HL configuration. The leading-edge devices along with the nacelle-pylon arrangement were shared with the CRM-SHL-AFC configuration as a result of the modular design. The simplified flap arrangement of the CRM-SHL-AFC configuration is shown in Fig. 2. The simple-hinged flap was fixed at 50° deflection and housed ten interchangeable AFC cartridges at the flap shoulder. This allowed for the fabrication of multiple, interchangeable cartridges per spanwise location, such that distinct AFC techniques might be evaluated. Ten AFC cartridges, four on the inboard and six on the outboard, are enumerated in sequential order, where the most inboard cartridge is designated as C1 and the most outboard is designated as C10 (left image of Fig. 2). The focus of this paper will be on unsteady pressure measurements made over the simple-hinged flap using the High Efficiency Low Power (HELP) actuators, which consisted of unsteady, sweeping-jet blowing for Row 1 and steady, discrete-jet blowing for Row 2 (right image of Fig. 2). Detailed discussions on the different AFC actuators may be found in Lin et al. [1,2].

Detailed views of the CRM-SHL-AFC flaps are shown in Fig. 3. The ten AFC cartridges can be seen as well as the locations of the twelve piezoresistive pressure transducers. Each dark square indicates the presence of a transducer, and the channel numbers are listed below each location. The twelve sensors were mounted in six rows. Each row consisted of two transducers, one located just downstream of an AFC cartridge and the second located near the trailing-edge of the flap. Even numbered channels were located downstream of the AFC cartridge, and odd channel numbers were positioned near the trailing edge. Depending on the location of the transducer, the sweeping frequency of the individual actuators could be identified in the spectra. Table 1 presents the reference coordinates for the SHL unsteady pressure transducers. There were also six transducers mounted on or near the wingtip and another seven on the nacelle pylon. These sensors were installed to satisfy acoustic testing requirements [5].

The coordinate system shown in Table 1 is the standard orthogonal system. X is in the streamwise direction, Y is in the tunnel wall-normal direction, and Z is in the direction normal to the plane formed by the main element of the wing. For reference, the fuselage nose is located at x = 9.3 in., y = 0 in., z = 19.8 in. As shown in Fig. 3, Channel 0 is located closest to the root of the wing just downstream of the most inboard AFC cartridge, while Channel 1 is located along the same row near the flap trailing-edge. Channel 2 is on the next row moving outboard, just downstream of the third cartridge. And the pattern continues upward to the most outboard row of transducers, which is located downstream of the tenth AFC cartridge.

IV. Data Acquisition and Analysis of the Unsteady Pressures

The differential pressure transducers had a full-scale range of 5 psid and a nominal sensitivity of 550 mV/psid. Each of the sensors was referenced to facility ambient pressure. The frequency response of each transducer was flat from DC to 20 kHz as stated from the manufacturer [6]. The frequency response of each transducer was also independently verified following the procedure documented in Ref. [7]. The specific transducers employed an A-Screen, which is essentially a simple hole on the order of the sensor diameter. The physical size of each sensor is 500 by 500 micrometers. Minimal attenuation due to the finite size of the sensor is shown to exist from estimates provided by the manufacturer concerning spatial resolution [6].

Table 1 Reference coordinates for the unsteady pressure transducers.

Channel #	X (in)	Y (in)	Z (in)
0	142.195	18.539	15.458
1	144.761	19.608	11.295
2	144.104	28.846	17.488
3	146.73	29.901	13.413
4	145.753	39.167	19.332
5	148.389	40.217	15.281
6	149.944	49.156	20.719
7	152.506	50.502	17.318
8	158.659	64.592	22.364
9	160.899	65.754	19.42
10	167.179	80.159	23.77
11	169.011	81.114	21.379

The raw voltages from the pressure transducers were AC-coupled at 0.25 Hz and had a cutoff filter applied at 20 kHz using an 8th-order low pass filter. The cutoff frequency corresponded to the usable frequency bandwidth as determined by the manufacturer [6]. Satisfying the Nyquist sampling criterion resulted in a sampling frequency of 50 kHz. Each channel was digitized using a 16-bit A-to-D converter at the required sampling rate. Data from all the channels were taken simultaneously, and the total record length of each channel was set to twenty seconds resulting in one million samples per channel.

The pressure transducers were calibrated in situ with a known pressure that was applied through the reference port of the sensors. The sensor response is essentially linear within the stated full-scale range, so the calibration slope determined the sensitivity that would be applied to the voltage signal in order to generate a time history of the fluctuating pressure. Autospectral density estimates were obtained through application of the Welch method using a Hanning window with 50% overlap. The Welch method is effectively a moving average, and a total of 200 blocks were used to reduce uncertainty in the resulting spectra [8]. Each block average was comprised of 5000 data samples, and the spectral resolution for the data set was 10 Hz.

V. Uncertainty

Uncertainty of the second-order moment pressure fluctuations will be presented in RMS form in an attempt to quantify errors in the data acquisition process. The basic assumption of the analysis was that error propagates through the system in an RMS fashion [9]. The analysis for the current data set was based on previous work that involved unsteady pressure measurements in a study investigating the flow field of a wing-fuselage juncture [10]. Findings from the current investigation show that the dominant error source was the variance of the voltage signal from the pressure transducer. This variance was estimated based on the difference between higher-order moments computed from the individual voltage signals [11].

Following the procedure set forth by Kegerise and Neuhart [10], the unsteady pressure is defined as a function of the sensor sensitivity and voltage, and also the filter gain:

$$p(t) = \frac{sv(t)}{G} \tag{1}$$

In this equation, *s* is the sensitivity in units (psi / V), *v* is the sensor voltage in units (V), and G is the nondimensional filter gain. The following equation is derived by applying the concepts in Coleman and Steele [6], and the actual derivation may be found in Kegerise and Neuhart [10]:

$$U_{\overline{p^r}}^2 = r^2 \left(\frac{s^{r-1}}{G^r} \overline{v^r} \right)^2 U_s^2 + r^2 \left(\frac{s^r}{G^{r+1}} \overline{v^r} \right)^2 U_G^2 + \left(\frac{s}{G} \right)^{2r} U_{\overline{v^r}}^2 \tag{2}$$

For the current investigation, the uncertainty due to gain was found to be negligible. The uncertainty due to the transducer sensitivity was found to be a second-order effect at best. Kegerise and Neuhart quote a value of +/- 1.35% for this uncertainty, which was obtained through Monte-Carlo simulations [10]. For the current investigation, multiple sensor calibrations were performed in order to estimate the sensitivity uncertainty [9]. A value of +/- 1.58% was determined and is comparable to the estimate from Kegerise and Neuhart. Note that the worst-case calibration error from a single transducer was used to determine the sensitivity uncertainty for the current study.

The dominant error term is the variance of the sensor voltage and is defined as follows [11]:

$$\text{var}\left(\overline{v^2}\right) = \frac{1}{N}\left(\overline{v^4} - \overline{v^2}^2 + 4\overline{v}^2\,\overline{v^2} - 4\overline{v^3}\,\overline{v}\right) = \frac{1}{N}\left(\overline{v^4} - \overline{v^2}^2\right) \tag{3}$$

In this equation, *N* represents the number of independent samples, not the total number of samples acquired. From a practical perspective, the number of independent samples may be estimated by examining the first zero-crossing of the autocorrelation computed from the unsteady pressure data. Mathematically, the integral time scale determines the smallest time step between two independent samples. Dividing the total record length by twice the integral time scale will lead to an estimate of N. Table 2 presents the worst-case RMS uncertainties for the fluctuating pressures from run 103, point 1605 (α = 16°, NPR = 2.35). The work of Kegerise and Neuhart shows the complete derivation of the equations used to obtain uncertainty estimates for the micro-machined piezoresistive pressure transducers [10].

Table 2 RMS pressure uncertainties for M = 0.2, α = 16°, NPR = 2.35.

Channel #	Calibration Slope (V/psi)	Uncertainty (%)
0	0.5508	1.64
1	0.5440	6.31
2	0.5471	1.80
3	0.5509	5.70
4	0.5523	1.40
5	0.5472	1.83
6	0.5489	1.79
7	0.5499	4.75
8	0.5517	0.86
9	0.5445	2.00
10	0.5484	0.92
11	0.5463	1.51

VI. Results

The complex nature of the flow over the simple-hinged flaps is demonstrated in Figs. 4 and 5. Flow conditions for these data are Mach number of 0.2, nominal NPR of 2.34, and angle of attack of 8° (without wall corrections). Computations from Vatsa show alternating regions of attached and separated flow over the flaps [12]. The computational patterns are qualitatively similar to experimental results found in flow visualizations made during the Fall 2018 entry [1]. The flow visualization is presented in three sections along the flap as seen in Fig. 5. The first section (Fig. 5a) covers the inboard flap and AFC cartridges C1-C4. The flow patterns over the outboard flap follow (Figs. 5b and 5c). The complex nature of the flow and large regions of separation make interpretation of the single-point unsteady pressure data difficult. As spectra from each unsteady sensor are presented, an attempt will be made to

identify the region of flow in which each sensor is located. The power spectral density of the fluctuating pressure (G_{pp}) has been normalized by the tunnel dynamic pressure (Q) and is presented in units of 1/ Hz.

The sensor noise floor was consistent throughout the test and was used to monitor the health of the unsteady pressure transducers. An example is given in Fig. 6. These spectra are typical of that obtained throughout the test entry from wind-off data points. Note that the run and point numbers for the data are included in the plot legends for reference. The small peak at 60 Hz is to be expected and indicates the presence of a ground loop. The small, distinct peak just above 1 kHz was present for a few days during the entry, and while troubleshooting was attempted, no consistent source could be identified. The broad peak just shy of 20 kHz was due to the addition by the manufacturer of in-line amplifiers in the cables six feet downstream of the transducers. The usable bandwidth for these measurements was on the order of 20 KHz. In most cases, the noise floor was significantly lower than the signal obtained during wind-on tunnel operation.

Baseline data were taken for the CRM-SHL-AFC configuration with AFC off. Note that the leading-edge devices along with the nacelle-pylon arrangement were also part of the CRM-SHL-AFC configuration (Fig. 1), and the data were taken at a Mach number of 0.2. Baseline spectra are presented for $\alpha = 0°$ in Fig. 7 and $\alpha = 16°$ in Fig. 8; no wall corrections were applied to the data in either case. Repeatability of the spectra was evaluated using multiple baseline runs (Runs 52, 55, 74, and 117) made over a three-week period. Note that the AFC cartridges were taped over during Run 55 to ensure that the AFC system produced no flow when the NPR was assumed to be constant at 1.0. The broad peak near 20 kHz is believed to be noise due to inline amplification and can be seen in Fig. 7. In general, good repeatability was achieved for the baseline (AFC-off) data shown in Figs. 7 and 8.

The outboard flap and the inboard flap feature a ~30° and a ~10° sweep angle, respectively. Because of the high flap deflection (50°), both inboard and outboard flaps contained extensive and massive flow separation for the AFC-off case (NPR = 1) where the outboard flap embodied more 3D flow features due to the spanwise flow component than that seen on the inboard flap [1,2,12]. For the most outboard location at the flap shoulder (Channel 10), Fig. 7 shows a spectral peak around 120 Hz that could be associated with the 3D flow separation on the outboard flap previously reported. The inboard location (Fig. 8) does not show this definitive frequency peak, though the flow may well be separated. Spectra from both figures demonstrate the difficulty of interpreting point-source data in the presence of a highly separated, 3D flow field.

Repeatability of the measurements with AFC on was evaluated at two different NPR settings for the HELP actuators. The first NPR setting was 1.25 and these spectra are presented at $\alpha = 8°$ in Fig. 9 for Channel 3. This sensor was located near the middle of the inboard flap, downstream of AFC Cartridge 3, and just upstream of the flap trailing edge (Fig. 3). The second NPR setting was 1.5 and these spectra are presented at $\alpha = 16°$ in Fig. 10 for Channel 8. This sensor was located near the middle of the outboard flap and just downstream of Cartridge 8 (Fig. 3). All the data were taken on the CRM-SHL-AFC configuration at $M = 0.2$. In general, good repeatability was achieved at both NPR settings. Figure 9 presents a spectral signature from a sensor located just upstream of the flap trailing edge that is somewhat typical of most odd number channels. Compared to the AFC-off case (Fig. 8), there are similarities in the shape of the spectra, but the spectra levels are higher for the AFC-on case presumably due to the AFC actuation and increased turbulent kinetic energy associated with greater flow circulation over the flap.

Figure 10 demonstrates some interesting characteristics associated with this highly 3D flow field over the outboard flap. Channel 8 was located just downstream of AFC cartridge 8 in the middle of the outboard flap. The broad peak around 100 Hz documents a large periodic event. Flow visualization from Fig 5(c) shows that this sensor appears to sit in a location near a separated flow region and in the presence of an imposed cross flow. The flow visualization was made at $\alpha=8°$ and NPR=2.34 while the data were taken at $\alpha=16°$ and NPR=1.5. The lower NPR combined with the higher angle of attack suggests that the 3D separated region may be encroaching upon the sensor. The broad peak around 100 Hz may be a quantification of the oscillatory nature of the 3D flow field as flow through the unactuated gap between cartridges infringes upon the attached flow region behind the AFC cartridge.

Figure 10 also shows a spectral peak at around 1400 Hz. This is in agreement with the measured oscillating frequency of the Row 1 sweeping jets on the HELP actuators at NPR = 1.5 from a posttest benchtop measurement. The additional spectral peaks or minor humps observed at higher frequencies could represent higher harmonics of that fundamental frequency. Similarly, the spectral peaks associated with the Row 1 sweeping jets could be seen at all even numbered channels that were located immediately downstream of an AFC cartridge. The only exception is Channel 6, which was located just downstream of a small unactuated gap between Cartridges 5 and 6 (Fig. 3). Although not shown here, the data show that the measured oscillating frequency is slightly lower for channels just

downstream of the inboard actuators (Channels 0, 2, and 4) where the jet nozzles and AFC cartridges are a little larger than those located outboard.

The effect of NPR and angle of attack was documented for the CRM-SHL-AFC configuration as well. The data were taken at a Mach number of 0.2 with the HELP actuators. Alpha sweeps while holding NPR constant were generated for each unsteady pressure transducer. Figure 11 represents a typical result for a sensor located near the trailing edge. The broad, low-frequency peak shown here at approximately 80 Hz was relatively common, and an indication of flow separation near the flap trailing edge. The data shown were taken from Channel 5, which is located near the outboard edge of the inboard flap just upstream of the trailing edge at an average NPR of 2.34. As shown in Fig. 3, this pressure transducer sits in a large region of separated flow as observed from flow visualization in Fig. 5a. The measured broad frequency at around 80 Hz might also be the result of flow oscillations between the attached, AFC-induced wake and separated flow regions near the trailing edge.

In addition, NPR sweeps while holding angle of attack constant were also generated for each transducer. Figure 12 represents typical results for a sensor located immediately downstream of an AFC cartridge located on the inboard flap. As expected, the average sweeping frequency of the HELP actuators in Cartridge 4 increased as the NPR was raised (Fig. 12). In this case, the average actuator frequency varies from around 500 Hz for NPR = 1.12 to around 1100 Hz for NPR = 2.32.

Data used to generate the NPR and alpha sweeps were taken from six runs as listed in Table 3. The baseline run with NPR of 1.0 was the control case taken with no flow control. The table contains a listing of the run and point numbers, along with the angle of attack and NPR. A 12% spread in NPR values is seen in Run 102, which corresponds to a nominal NPR setting of 1.5. A 9% spread is observed in the data points from Run 103, which corresponds to a nominal NPR setting of 2.5. Roughly 10% spread from point to point seems to be the best that was achievable at the higher NPR values. And it was difficult to achieve the maximum NPR of 2.5 given the current experimental setup and compressor availability.

Table 3 Run and point numbers with testing parameters for data taken at $M = 0.2$.

Run	Point	Alpha	NPR Avg
74	954	0.000	1.000
74	956	4.000	1.000
74	959	8.000	1.000
74	963	12.000	1.000
74	968	16.000	1.000
108	1682	0.000	1.111
108	1684	4.000	1.113
108	1687	8.000	1.118
108	1691	12.000	1.116
108	1696	16.000	1.118
107	1658	0.000	1.239
107	1660	4.000	1.239
107	1663	8.000	1.244
107	1667	12.000	1.248
107	1672	16.000	1.285
102	1566	0.030	1.588
102	1568	4.030	1.609
102	1572	8.010	1.660
102	1576	12.010	1.464
102	1581	16.020	1.470
101	1539	0.000	2.086
101	1541	4.000	2.071
101	1544	8.000	1.941
101	1548	12.000	2.009
101	1553	16.000	2.096
103	1591	0.000	2.269
103	1593	4.000	2.286
103	1596	8.000	2.321
103	1600	12.000	2.467
103	1605	16.000	2.345

VII. Conclusion

Unsteady pressure measurements were made on the simplified high-lift configuration of the CRM. This configuration employed ten AFC cartridges to control large-scale separation over the simple-hinged flaps for lift enhancement. HELP actuators that used both steady blowing through discrete jets and oscillatory blowing through sweeping jets were employed to achieve this goal. The data acquisition process was documented and uncertainty of the unsteady pressure measurements quantified. In general, the repeatability of both AFC-on and AFC-off data was quite good. Spectra from sensors just downstream of the HELP actuators confirmed the expected sweeping-jet frequency of each cartridge and the associated increase in the sweeping frequency as the NPR was raised. For both AFC-on and AFC-off cases, sensors positioned near the trailing-edge of the flaps tend to display a somewhat "linear" decay of energy in the log-log scale region between 200 and 10,000 Hz. A broad-band frequency on the order of 80 Hz was also observed in the spectral signature for the AFC-on cases at the four stations farther from the wing root (Channels 5, 7, 9, and 11). This could be due to flow oscillations between the attached, AFC-induced wake and separated flow regions observed near the flap trailing edge.

Acknowledgments

This R&D effort was sponsored by the High Aspect Ratio Wing Subproject under the NASA Advanced Air Transport Technology (AATT) Project. The effort involved many people who provided valuable contributions through their hard work that made a successful test possible. The authors would like to thank all those involved for their great support during the course of this investigation.

References

[1] Lin, J. C., Melton, L. P., Hannon, J. A., Andino, M. Y., Koklu, M., Paschal, K. B., and Vatsa, V. N., "Wind Tunnel Testing of High Efficiency Low Power (HELP) Actuation for Active Flow Control," *AIAA SciTech 2020 Forum*, AIAA Paper 2020-0783, 2020. doi: 10.2514/6.2020-0783

[2] Lin, J. C., Melton, L. P., Hannon, J. A., Andino, M. Y., Koklu, M., Paschal, K. B., and Vatsa, V. N., "Testing of High-Lift Common Research Model with Integrated Active Flow Control," *Journal of Aircraft*, publish online August 25, 2020. http://arc.aiaa.org/doi/abs/10.2514/1.C035906

[3] Evans, A., Lacy, D., Smith, I., and Rivers, M., "Test Summary of the NASA Semi-Span High-Lift Common Research Model at the QinetiQ 5-Metre Low-Speed Wind Tunnel," *AIAA AVIATION 2020 Forum*, AIAA Paper 2020-2770, 2020. doi: 10.2514/6.2020-2770

[4] "NASA Aeronautics Research, 14- by 22-Foot Subsonic Tunnel Facility Overview," August, 2017. https://www.nasa.gov/aeroresearch/programs/aavp/aetc/subsonic/14x22

[5] Lockard, D. P., O'Connell, M. D., Vatsa, V. N., and Choudhari, M. M., "Assessment of Aeroacoustic Simulations of the High-Lift Common Research Model," *25th AIAA/CEAS Aeroacoustics Conference*, AIAA Paper 2019-2460, 2020. doi: 10.2514/6.2019-2460

[6] Hurst, A. M., Olsen, T. R., Goodman, S., VanDeWeert, J., Shang, T., "An Experimental Frequency Response Characterization of MEMS Piezoresistive Pressure Transducers," *Proceedings of ASME Turbo Expo 2014: Turbine Technical Conference and Exposition*, GT2014-27159, 2014. https://doi.org/10.1115/GT2014-27159

[7] Marcolini, M. A., Lorber, P. F., Miller, W. T., Jr., and Covino, A. F., Jr., "Frequency Response Calibration of Recess-Mounted Pressure Transducers," NASA Technical Memorandum 104031, March 1991. https://ntrs.nasa.gov/citations/19910012521

[8] Hardin, J. C., "Introduction to Time Series Analysis," NASA Reference Publication 1145, March 1986. https://ntrs.nasa.gov/citations/19860014920

[9] Coleman, H. W. and Steele, W. G., "Experimentation and Uncertainty Analysis For Engineers," John Wiley & Sons, Inc. 1989. doi:10.1002/9781119417989

[10] Kegerise, M. A. and Neuhart, D. H., "Wind Tunnel Test of a Risk-Reduction Wing/Fuselage Model to Examine Juncture-Flow Phenomena," NASA/TM-2016-219348, November 2016. https://ntrs.nasa.gov/citations/20160014854

[11] Benedict, L. H. and Gould, R. D., "Towards better uncertainty estimates for turbulence statistics," *Experiments in Fluids 22*, 1996, pp. 129-1136. doi: 10.1007/s003480050030

[12] Vatsa, V. N., Duda, B., Lin, J. C., Melton, L. P., Lockard, D. P., O'Connell, M., and Hannon, J. A., "Comparative Study of Active Flow Control Strategies for Lift Enhancement of a Simplified High-Lift CRM Configuration," *AIAA AVIATION 2019 Forum*, AIAA Paper 2019-3724, 2019. doi: 10.2514/6.2019-3724

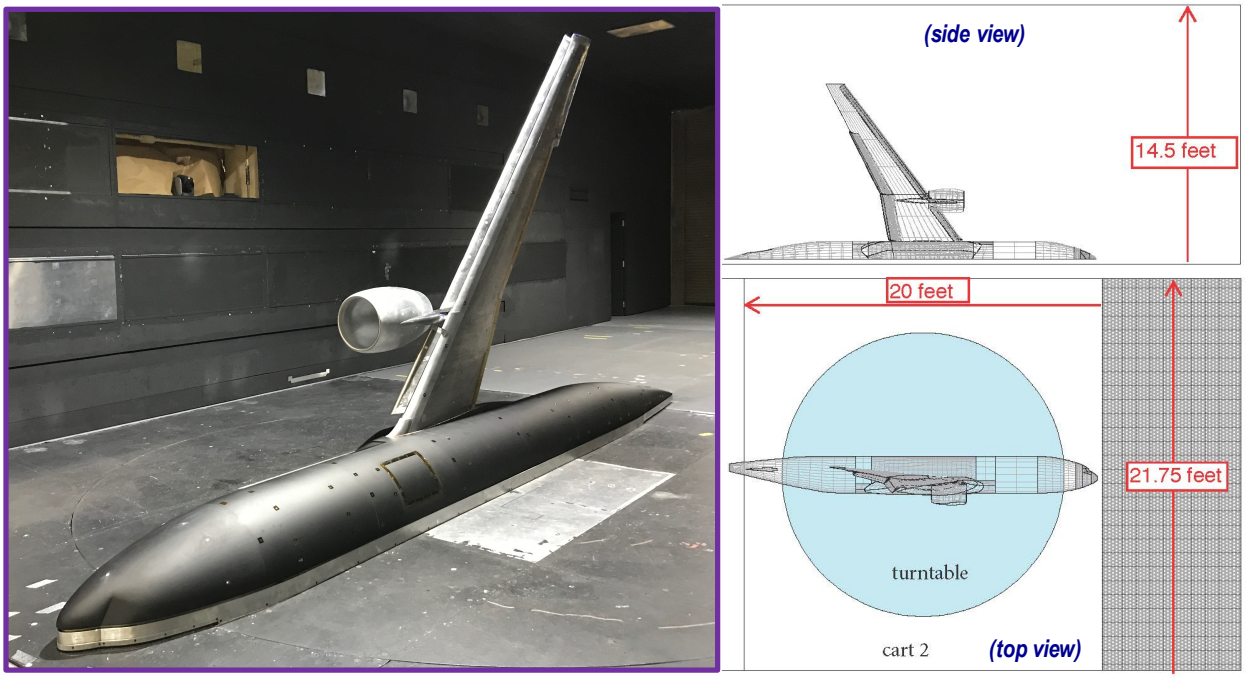


Fig. 1 CRM-HL configuration mounted in the 14x22.

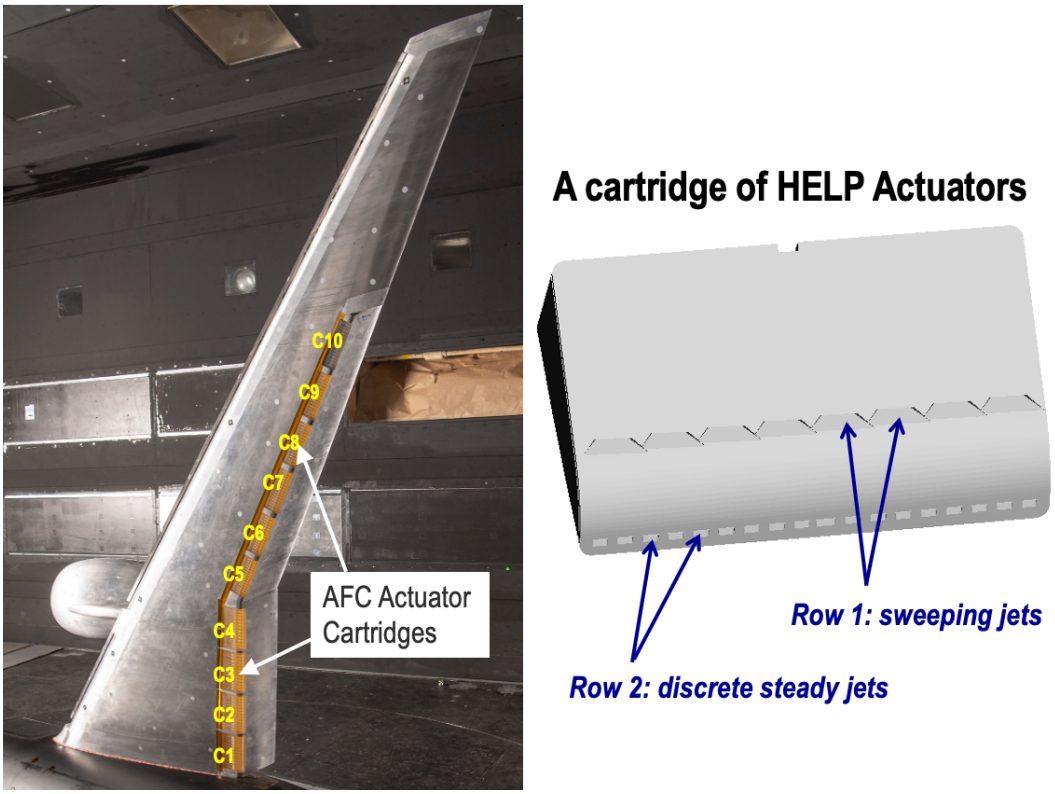


Fig. 2 CRM-SHL-AFC configuration mounted in the 14x22.

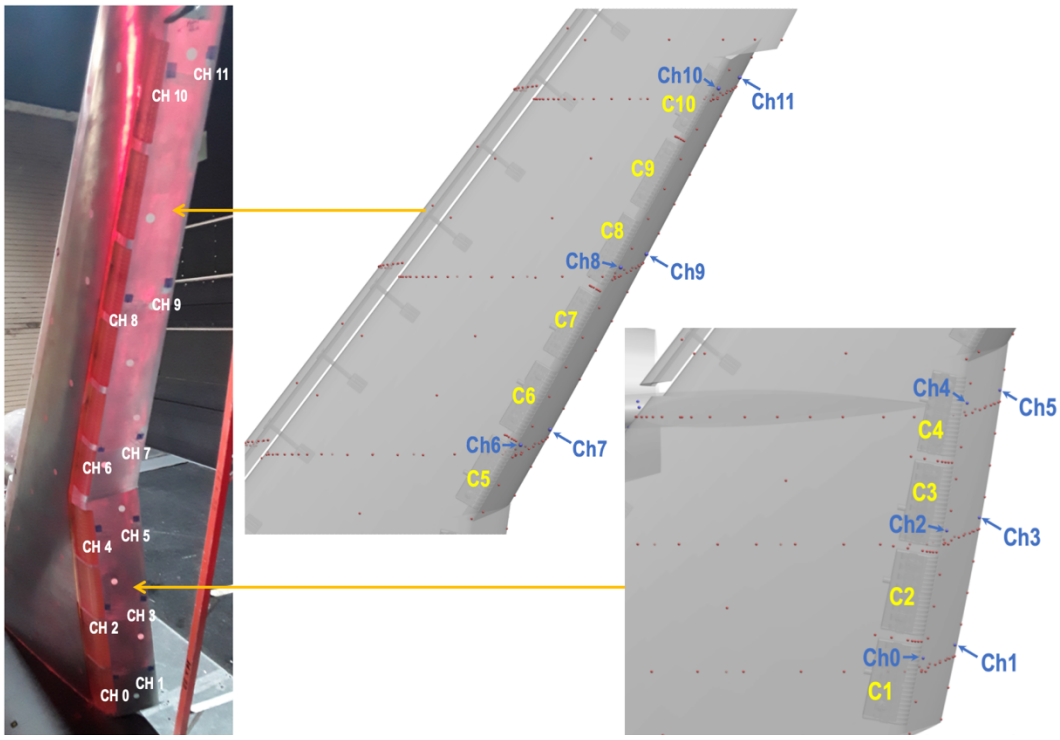


Fig. 3 CRM-SHL-AFC configuration with unsteady pressure transducer locations.

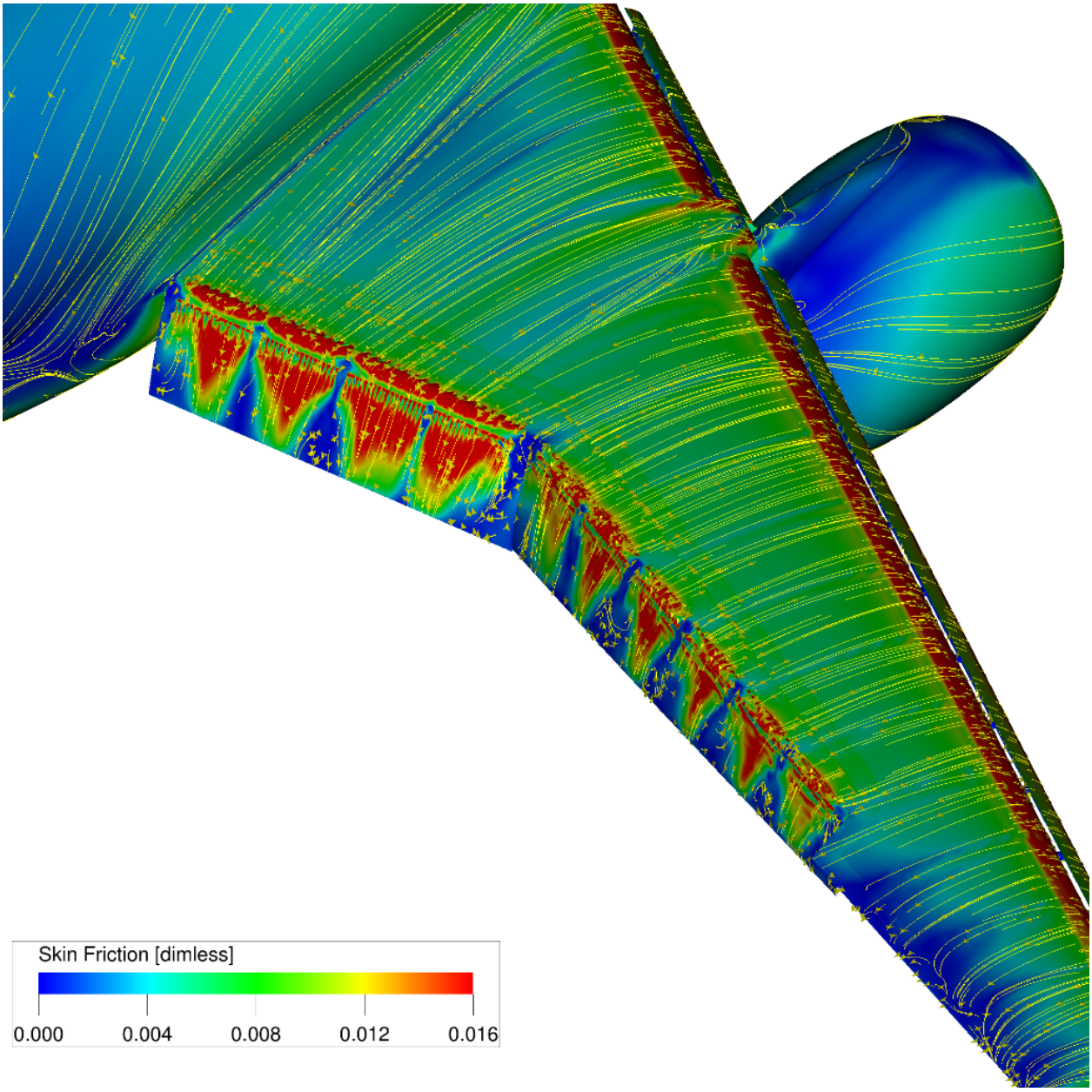


Fig. 4 Alternating regions of separated and attached flow (computations from Vatsa et al. [12]).

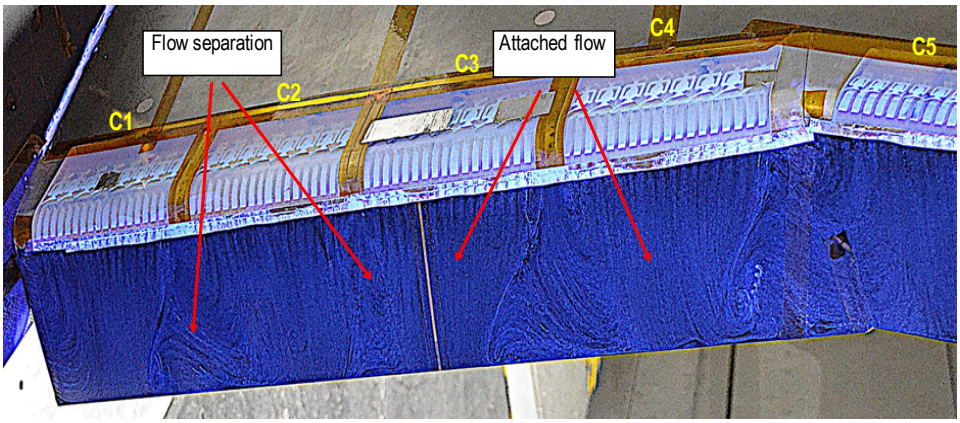


Fig. 5(a) Alternating regions of separated and attached flow C1-C4 (flow visualization from Lin et al. [1]).

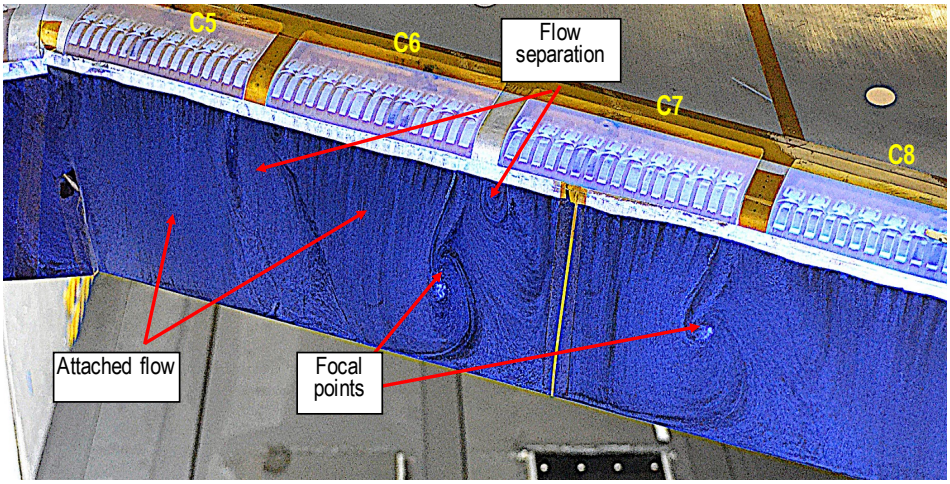


Fig. 5(b) Alternating regions of separated and attached flow C5-C7 (flow visualization from Lin et al. [1]).

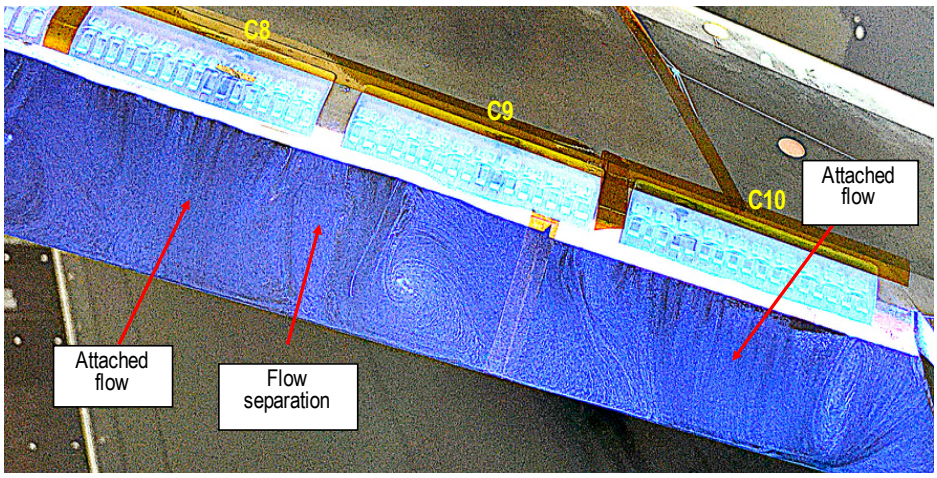


Fig. 5(c) Alternating regions of separated and attached flow C8-C10 (flow visualization from Lin et al. [1])

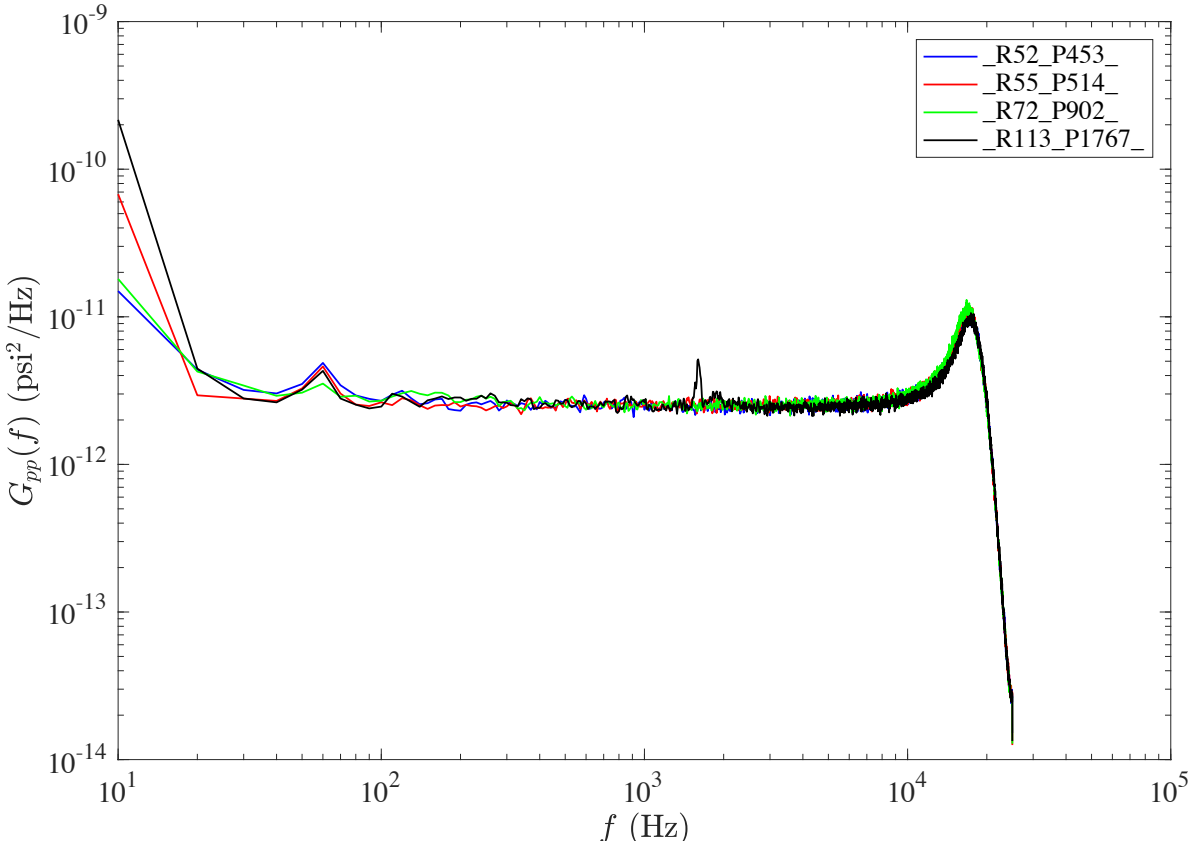


Fig. 6 Typical Spectra from wind-off data points representing the sensor noise floor.

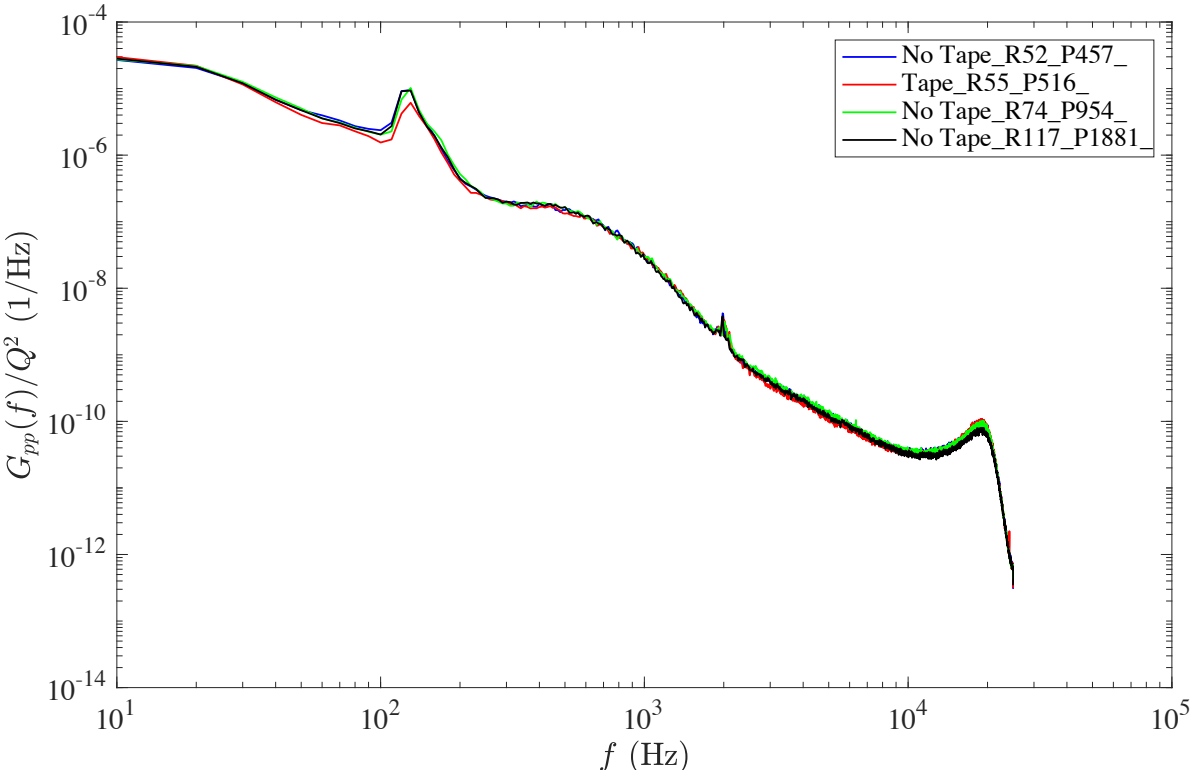


Fig. 7 Baseline spectra from Channel 10 at $\alpha = 0°$, $M = 0.2$, NPR = 1.0.

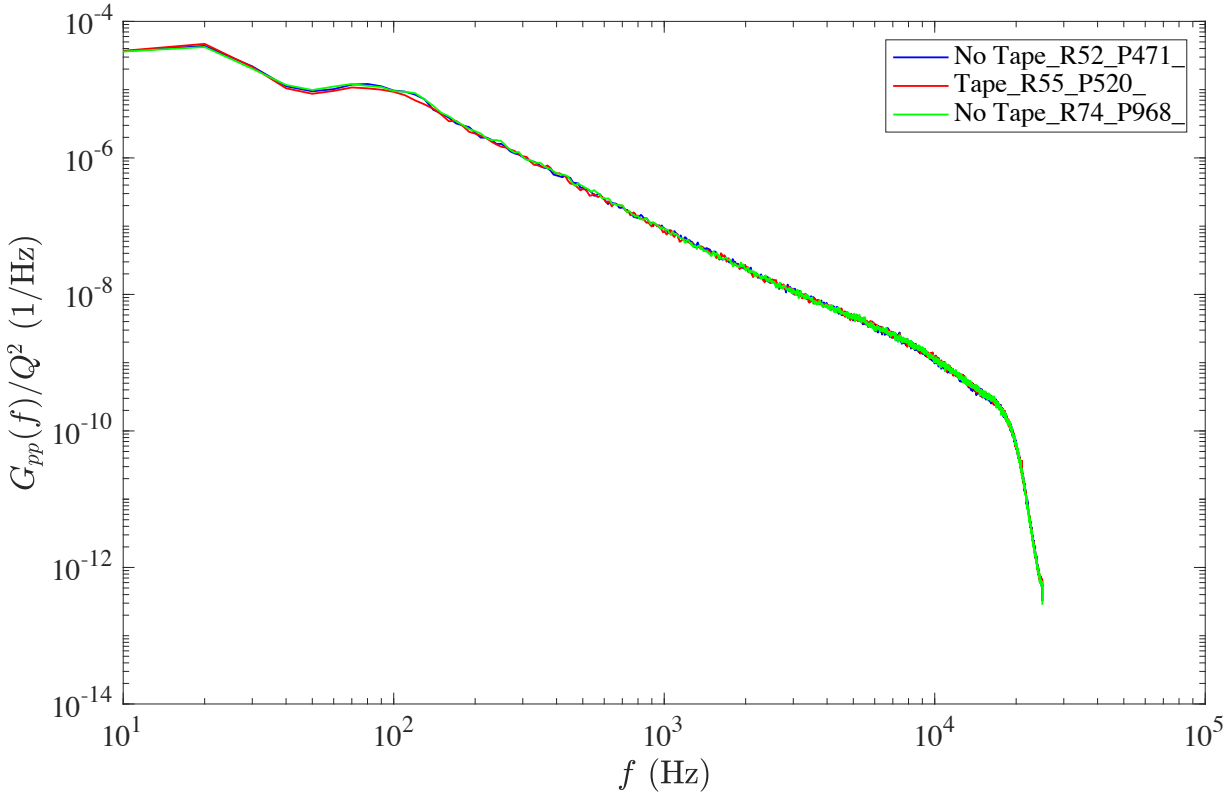


Fig. 8 Baseline spectra from Channel 1 at $\alpha = 16°$, $M = 0.2$, NPR = 1.0.

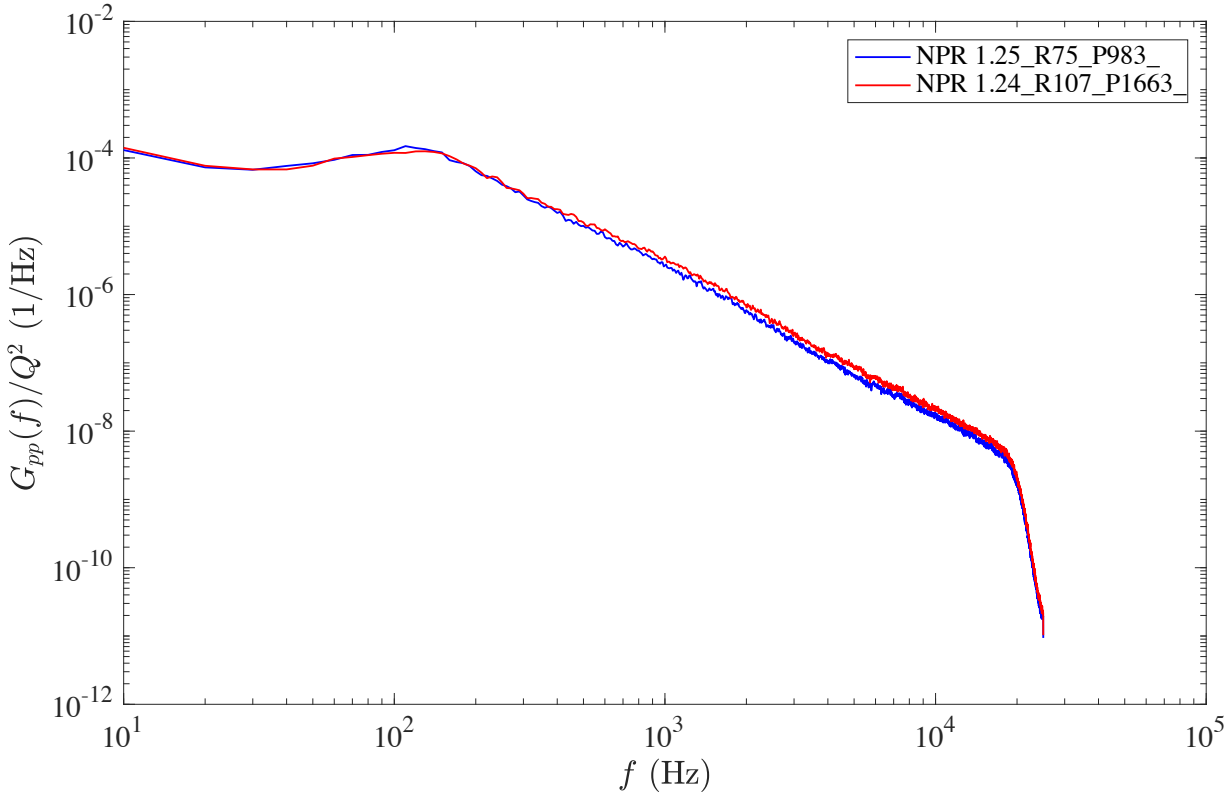


Fig. 9 Spectra from Channel 3 at $\alpha = 8°$, $M = 0.2$, NPR = 1.25.

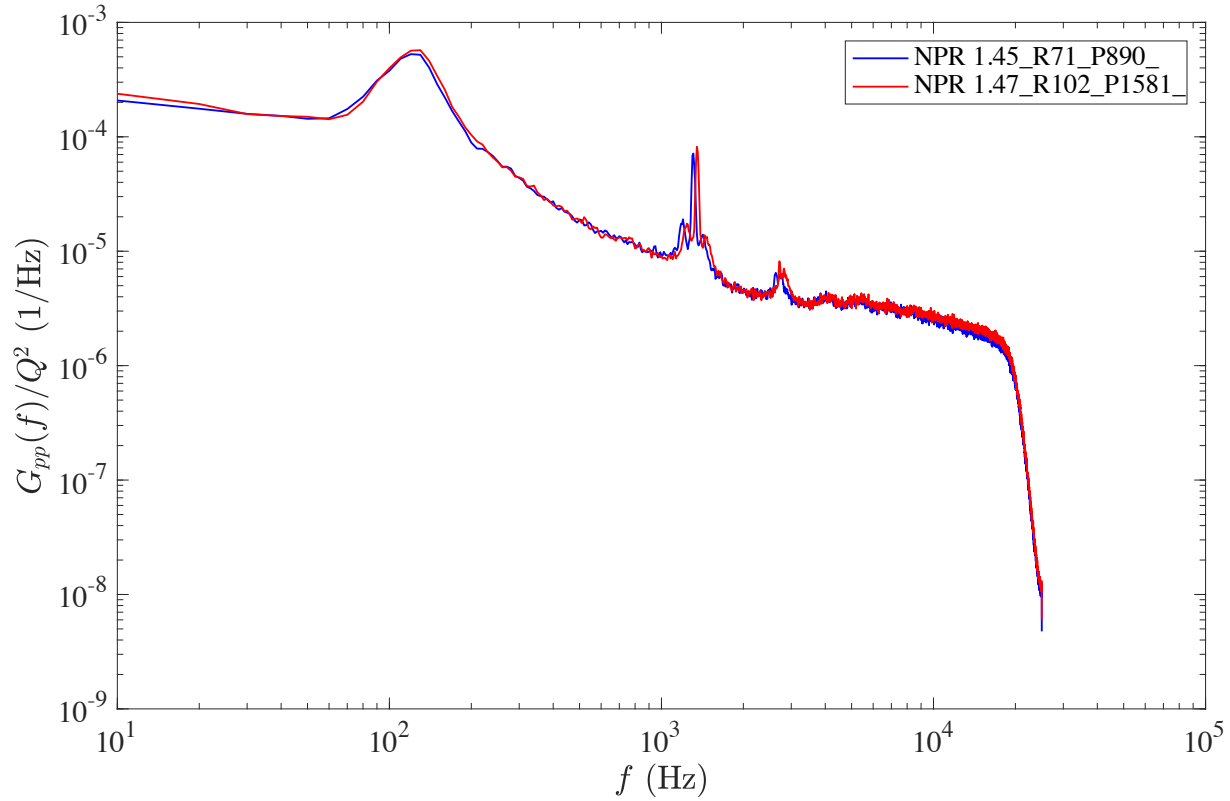


Fig. 10 Spectra from Channel 8 at $\alpha = 16°$, $M = 0.2$, NPR = 1.5.

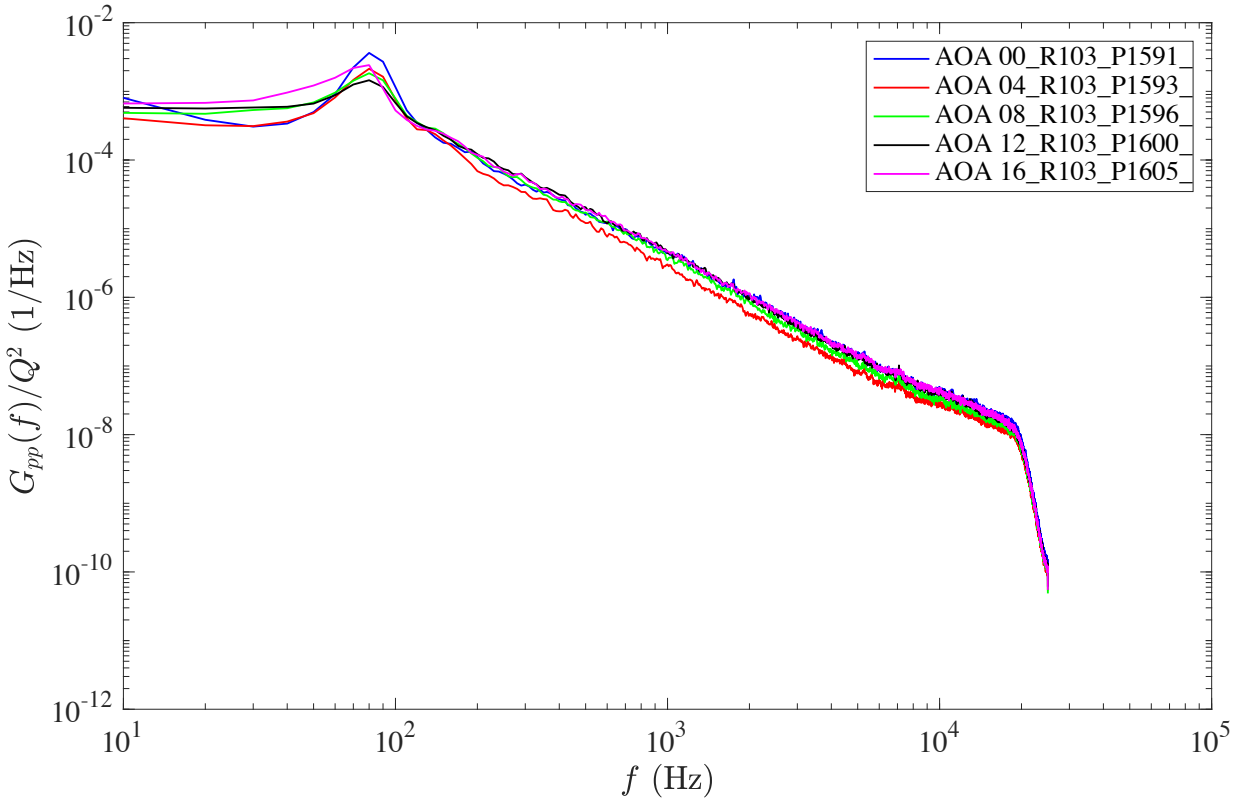


Fig. 11 Spectra from Channel 5 at $M = 0.2$ and NPR = 2.34.

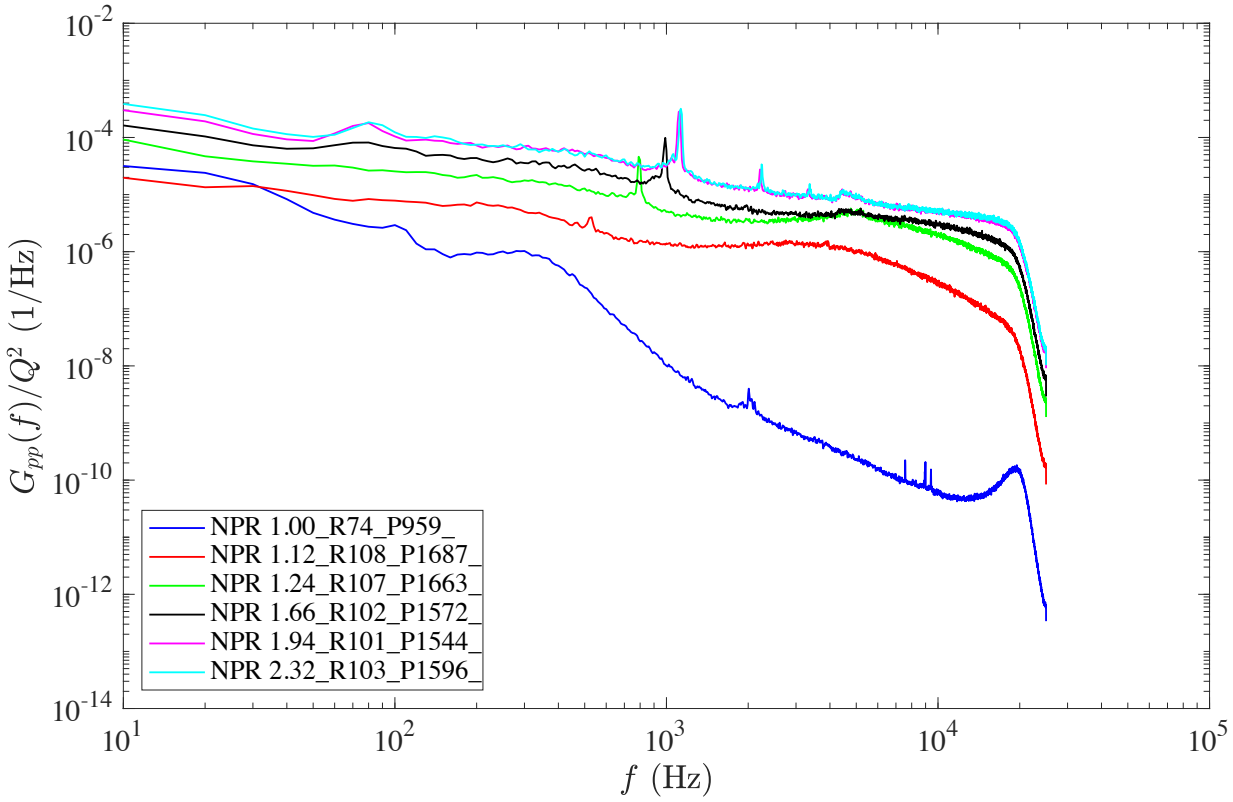


Fig. 12 Spectra from Channel 4 at $M = 0.2$ and at $\alpha = 8°$.